ACS MATERIALS LETTERS

www.acsmaterialsletters.org

LETTER

Nonuniform Debye Temperatures in Quasi-One-Dimensional Transition-Metal Trichalcogenides

Archit Dhingra, Alexey Lipatov, Michael J. Loes, Alexander Sinitskii, and Peter A. Dowben*

Cite This: *ACS Materials Lett.* 2021, 3, 414–419

Read Online

ACCESS | Metrics & More | Article Recommendations | Supporting Information

ABSTRACT: The Debye–Waller factor plots for S 2p core-level, based on temperature-dependent X-ray photoemission measurements on quasi-one-dimensional (1D) chains of TiS_3, suggest effective Debye temperatures of the two different types of sulfur coordination are 464 ± 35 K and 547 ± 26 K, respectively. The effective Debye temperatures for sulfur in ZrS_3 are found to be 558 ± 30 K and 667 ± 35 K, again, for the two different types of sulfur coordination. The differences in the Debye temperatures for the different sulfur species in both TiS_3 and ZrS_3, are consistent with the existence of inequivalent sulfur environments. Moreover, considerably higher Debye temperature for S 2p core-level of ZrS_3, in comparison with that of TiS_3, indicates that there is a likely decrease in phonon scattering of carriers in ZrS_3 compared to TiS_3. This conclusion is supported by a temperature-dependent maximum in the mobility for ZrS_3, that is at a higher temperature than seen for TiS_3 and a steeper decline in mobility for TiS_3, compared to ZrS_3. Because of the relatively high Debye temperatures, there are only a limited number of soft modes for the quasi-one-dimensional (1D) layered trichalcogenide semiconductors of TiS_3 and ZrS_3.

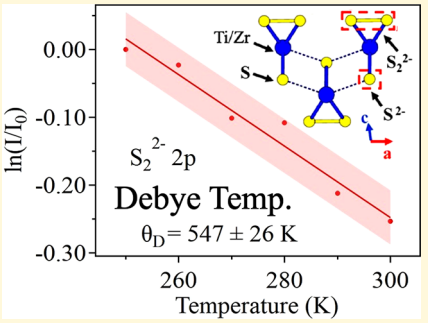

The thermal motion of atoms in a material leads to a decrement in the photoemission intensity, as well as a reduction in carrier mobility. Ascertaining the Debye temperature is important in the case of the transition metal trichalcogenides, because, despite the very high predicted carrier mobilities (~10 000 $cm^2 V^{-1} s^{-1}$ for TiS_3,[1] and ~1800–2500 $cm^2 V^{-1} s^{-1}$ for ZrS_3[2,3]), phonon scattering is now believed to be the source[4] of the low measured mobilities (~2–80 $cm^2 V^{-1} s^{-1}$ for TiS_3,[4−8] and ~10–30 $cm^2 V^{-1} s^{-1}$ for ZrS_3[9,10]). These low measured mobilities for TiS_3 are unlikely to be the result of contact problems, because the contacts are typically ohmic.[4,11] Therefore, determination of the Debye temperature would indicate whether the trichalcogenides, like TiS_3 and ZrS_3, are stiff and suffer from only a few soft phonon modes, or whether the lattice is quite soft and, thus, suppression of phonon scattering of the carriers would be difficult. Overcoating with Al_2O_3 increases the transistor carrier mobility in TiS_3 transistors,[12] suggesting that the suppression of soft modes is possible.

This understanding of the trichalcogenides, such as TiS_3 and ZrS_3, which are schematically shown in Figure 1, is important because of their potential electronic device applications. Two-dimensional (2D) materials comprising precise quasi-one-dimensional (1D) chains, namely, the transition-metal trichalcogenides (TMTs), offer an opportunity to fabricate a transistor <10 nm in width without significant edge scattering that will plague graphene and the transition-metal dichalcogenide (TMD) 2D semiconductors. The absence of edge disorder and dangling bond defects in TMTs, of the form MX_3 (where M = Ti, Ta, Zr, Hf, etc.; and X = S, Se, Te), is what makes the TMTs superior to graphene-based materials and TMDs. Defects are found to be responsible for considerable deterioration of electronic properties with reduction in channel widths[13−16] and hinder the scaling of TMDs and graphene-based materials down to 10 nm or less. However, mobilities that are more representative of the low effective carrier masses expected for trichalcogenides, such as TiS_3 and ZrS_3, would be very desirable.

Both TiS_3 and ZrS_3 are highly anisotropic[1,7,17] and strong *n*-type semiconductors with band gaps of ~1 eV (see refs 6, 18, and 19) and ~1.8–2.1 eV,[19−21] respectively. The modest band gap, along with a considerable predicted electron mobility,[1] make TiS_3, among the family of TMTs, a material of some

Received: February 8, 2021
Accepted: March 15, 2021

https://doi.org/10.1021/acsmaterialslett.1c00094
ACS Materials Lett. 2021, 3, 414–419

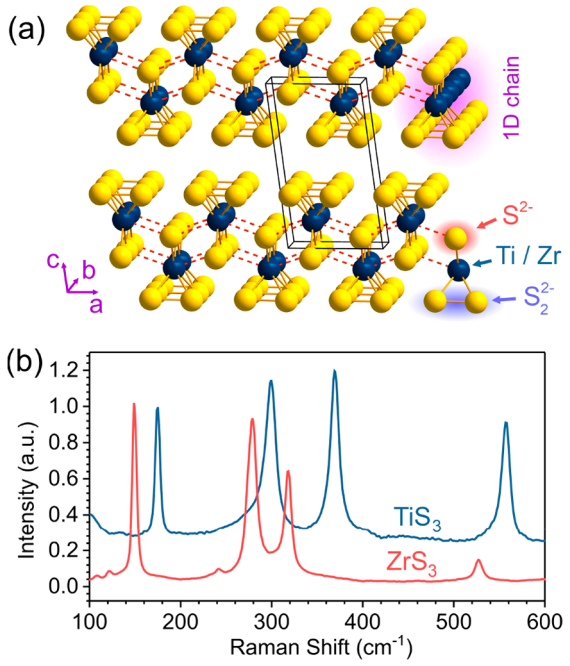

Figure 1. (a) Schematic of quasi-1D chains of TiS_3 (or ZrS_3), highlighting 1D chains and two different types of sulfur species (S^{2-} and S_2^{2-}). (b) Raman spectra of TiS_3 and ZrS_3.

interest. However, the presence of phonon scattering is deemed responsible not only for a significant reduction in a system's carrier mobility[4] (as mentioned above) but also for influencing the thermoelectric properties and phase stability. Here, we examine the thermal motion of sulfur atoms in TiS_3 and ZrS_3. The effective Debye temperature (which is a pivotal parameter for description of dynamic motion of atoms) for 2p core levels of the two distinct sulfur species, the sulfide (S^{2-}) and disulfide (S_2^{2-}), in TiS_3 and ZrS_3 (as identified in Figure 1a) were investigated using temperature-dependent X-ray photoemission spectroscopy (XPS).

Synthesis of TiS_3 nanowhiskers was achieved by a direct reaction of vapors of sulfur with metallic titanium in vacuum-sealed quartz ampules heated to 550 °C, as described in previous literature.[22−24] Nanowhiskers of ZrS_3 were synthesized by making metallic zirconium react with sulfur vapors in vacuum-sealed quartz ampules at a higher temperature (800 °C).[25,26] TiS_3 and ZrS_3 are isostructural crystals that belong to the $P2_1/m$ space group. The lattice constants for TiS_3 are a = 4.9728(6) Å, b = 3.4055(4) Å, c = 8.8146(15) Å, and β = 97.56(1)°; whereas the lattice constants for ZrS_3 are a = 5.1107(4) Å, b = 3.6179(2) Å, c = 8.9725(5) Å, with the cant angle being β = 97.64(1)°, as described elsewhere.[20]

The temperature-dependent S 2p core-level XPS measurements were performed in an ultrahigh vacuum (UHV) chamber, using a SPECS X-ray Al anode ($h\nu$ = 1486.6 eV) source and a hemispherical electron analyzer (PHI Model 10−360), which has an angular acceptance of ±10°. The TMT nanowhiskers were cooled between 250−300 K using a liquid nitrogen cryostat that was connected to the sample holder, as described in our previous work.[27]

Raman spectra were measured at room temperature with a Thermo Scientific DXR Raman microscope using a 532 nm excitation laser. The Si band at 520 cm^{-1} was used as the Raman shift reference.

Typical Raman spectra of TiS_3 and ZrS_3 crystals are shown in Figure 1b. For TiS_3 we observe four A_g Raman-active modes at ω_{Ti}^{I} = 175 cm^{-1}, ω_{Ti}^{II} = 300 cm^{-1}, ω_{Ti}^{III} = 369 cm^{-1}, and ω_{Ti}^{IV} = 557 cm^{-1}, which correspond to I (A_g^{rigid}), II ($A_g^{internal}$), III ($A_g^{internal}$), and IV (A_g^{S-S}), respectively.[22,28] Similar peaks for ZrS_3 are observed at ω_{Zr}^{I} = 149 cm^{-1}, ω_{Zr}^{II} = 279 cm^{-1}, ω_{Zr}^{III} = 318 cm^{-1}, and ω_{Zr}^{IV} = 527 cm^{-1}, and are consistent with the previous studies.[34] The shift of ZrS_3 peaks to lower frequencies is attributed to a 1.9 times higher atomic mass of Zr, compared to Ti. The oxidized crystals would be expected to exhibit additional Raman peaks at 225 and 360 cm^{-1} for ZrS_3,[29] or at 150 and 395 cm^{-1} for TiS_3.[30] The absence of these peaks indicates the high quality of the crystals used in this work.

Figure 2 shows representative XPS spectra of the S 2p core level collected at 250 and 290 K for both systems, and, as

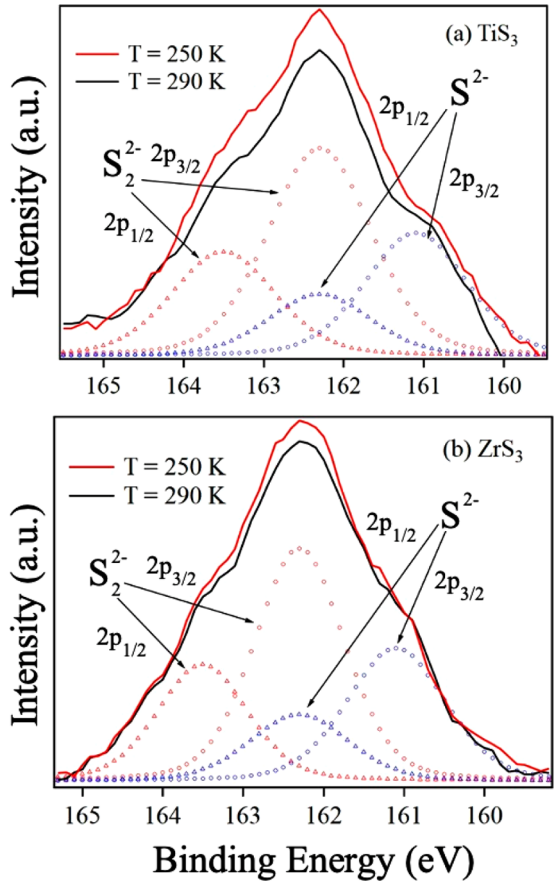

Figure 2. Photoemission spectra of the S 2p core levels for (a) TiS_3 and (b) ZrS_3. The solid lines represent the raw spectra collected at 250 K (solid red) and 290 K (solid black), whereas hollow triangles and circles indicate the fit to the spectra collected at 250 K. The $2p_{1/2}$ contribution to the core-level photoemission intensity is shown by hollow triangles (blue for S^{2-} $2p_{1/2}$ and red for S_2^{2-} $2p_{1/2}$), while the $2p_{3/2}$ contribution is indicated by hollow circles (blue for S^{2-} $2p_{3/2}$ and red for S_2^{2-} $2p_{3/2}$).

expected, the photoemission intensities are somewhat temperature-dependent. Photoemission is regarded as a scattering process, where the vibrational amplitudes of the scattering centers contribute to indirect phonon-assisted transitions and lead to a decrease in the photoemission spectral intensity with increasing temperature.[31,32] As noted elsewhere,[11,23] the S 2p core-level features for both TMTs contain four components,

https://doi.org/10.1021/acsmaterialslett.1c00094
ACS Materials Lett. 2021, 3, 414−419

with two of them (S^{2-} $2p_{1/2}$ and S_2^{2-} $2p_{3/2}$) overlapping at 162.3 eV while the remaining components are at 161.1 eV (S^{2-} $2p_{3/2}$) and 163.5 eV (S_2^{2-} $2p_{1/2}$).

The decrease in the XPS photoemission intensities, with increasing temperature, is an expected consequence of direct temperature dependence of the Debye−Waller scattering (i.e., the vibrational modes and amplitude of the atoms normal to the surface)[31,32] for both of the trichalcogenides. The quantitative relationship between XPS intensities and the effective Debye temperature of a given system can be established through the Debye−Waller model. The photoemission intensity, in XPS, will show an exponential decrease with an increase in temperature. This exponentially decaying function is characterized by the system's Debye−Waller factor ($W(T)$) and is expressed as[27,31−35]

$$I = I_0\, e^{-2W(T)}$$

For isotropic vibrations, $W(T)$ is given by[27,31−35]

$$W(T) = \frac{3(\hbar\Delta k)^2 T}{2mk_B{\theta_D}^2}$$

Here, T is the temperature, m the mass of the scatterer, k_B is the Boltzmann constant, $(\hbar\Delta k)$ is the electron momentum transfer, and θ_D is the effective Debye temperature. The value of θ_D depends on the slope (S) of the Debye−Waller plots shown in Figure 3; θ_D is expressed as

$$-S = \frac{3(\hbar\Delta k)^2}{mk_B{\theta_D}^2}$$

In the geometry of this experiment, the photoemission intensity is dominated by vibration modes normal to the surface, not in-plane or anharmonic modes,[31,32] as noted above. So the Debye temperature extracted from the data is only an effective Debye temperature but can be, nonetheless, compared to other measures of the Debye temperature.[27,31,35] From slope of the plots in Figure 3a, the effective Debye temperatures of the S^{2-} 2p and S_2^{2-} 2p core levels of TiS_3 are estimated to be 464 ± 35 K and 547 ± 26 K, respectively. Likewise, the slopes of Debye−Waller plots in Figure 3b give effective Debye temperatures of the S^{2-} 2p and S_2^{2-} 2p core levels of ZrS_3 as 558 ± 30 K and 667 ± 35 K, respectively. As expected, the effective Debye temperatures of the different sulfur species S^{2-} and S_2^{2-}, from the 2p core-level photoemission, differ consistently for both TiS_3 and ZrS_3. These differences in S^{2-} and S_2^{2-} Debye temperatures are expected from the differences in sulfur coordination in the trichalcogenide. Since higher coordination implies greater lattice stiffness, the Debye temperature of the disulfide bridging S_2^{2-} sulfur in the TMTs is expected to be higher than that of the S^{2-} sulfur, as is observed. The higher effective Debye temperatures for the S^{2-} and S_2^{2-} for ZrS_3 than for TiS_3 can be explained by the fact that the Zr−S bonds are more ionic in nature than the Ti−S bonds, which, in turn, renders the ZrS_3 lattice the stiffer of the two TMTs, despite the fact that the Raman modes are at lower energy for ZrS_3 than TiS_3, as seen in Figure 1b.

Even though the effective sulfur Debye temperature of TiS_3 is found to be lower than that of ZrS_3, it is still considerably higher than the effective surface Debye temperature of another well-studied TMT, namely, In_4Se_3.[27] More importantly, these relatively high Debye temperatures measured here suggest that the TiS_3 and ZrS_3 lattices are, overall, quite stiff. This means

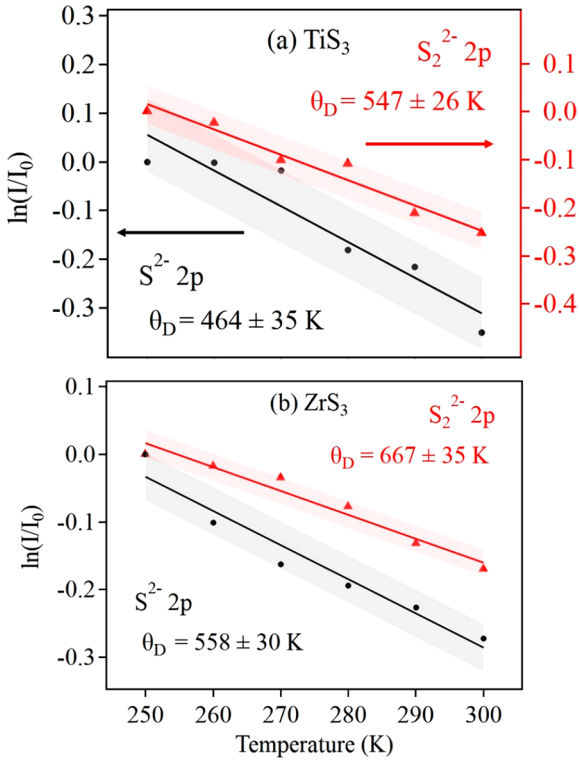

Figure 3. Debye−Waller factor plots ($\ln(I/I_0)$ vs temperature) for (a) the sulfur S^{2-} 2p (gray) and S_2^{2-} 2p (red) core-level components of TiS_3 and (b) the sulfur S^{2-} 2p (gray) and S_2^{2-} 2p (red) core-level components of ZrS_3. The effective Debye temperatures for the S^{2-} and S_2^{2-} 2p core levels for TiS_3 are 464 ± 35 K and 547 ± 26 K, respectively, while the effective Debye temperatures for the S^{2-} and S_2^{2-} 2p core levels for ZrS_3 are 558 ± 30 K and 667 ± 35 K, respectively.

that these systems have relatively fewer soft modes, of which some can be seen in the measured Raman spectra (Figure 1b). The fact that there may only be a limited number of soft modes means that the suppression of carrier scattering by phonons can be, quite plausibly, realized.

To supplement the Debye temperature measurements, we analyzed the temperature-dependent field-effect mobilities for both TiS_3 and ZrS_3. The temperature-dependent transistor mobilities, previously measured for TiS_3,[4] can be compared to the transistor mobilities for ZrS_3. To do this, a ZrS_3 device was fabricated based on a few-layer ZrS_3 crystal (width (w) = 2.2 μm, thickness (t) = 12 nm) exfoliated on a Si/SiO_2(300 nm) substrate, with metal contacts (3 nm of Cr, 45 nm of Au) separated by 10.0 μm. This device is comparable to the previously reported few-layer TiS_3 device (t = 6.8 nm, w = 125 nm, with two Cr/Au electrodes separated by 5.1 μm) with reported temperature-dependent field-effect mobility measurements.[4] In the field-effect electrical measurements, the Cr/Au contacts served as source (S) and drain (D) electrodes, while the conducting p-doped Si served as the bottom gate (G) and SiO_2 layer served as the gate dielectric. The measurements were performed in the temperature range of 77−305 K. The field-effect mobilities were extracted from the $I_{DS}-V_G$ curves.

Figure 4 shows a comparison of temperature-dependent field-effect mobilities for TiS_3[4] and ZrS_3 at the same gate voltage of 10 V. While the temperature dependence of the band bending can lead to the conduction band dropping below the Fermi level, as seen for some trichalcogenides,[36] an applied

https://doi.org/10.1021/acsmaterialslett.1c00094
ACS Materials Lett. 2021, 3, 414−419

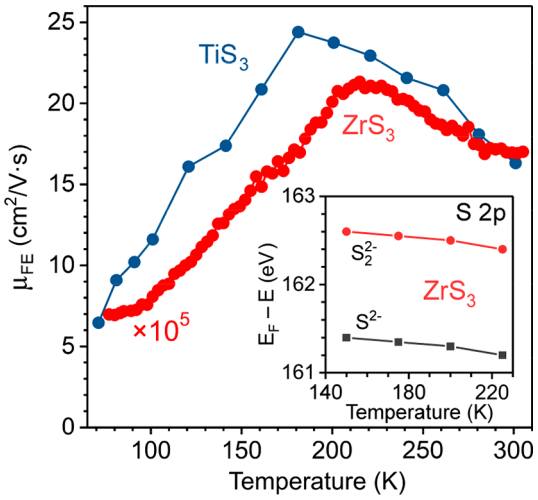

Figure 4. Field-effect mobilities for TiS_3 (blue) and ZrS_3 (red) at a gate voltage of 10 V. The mobilities for ZrS_3 are ~10^5 smaller than that for TiS_3 and have been rescaled as indicated. The TiS_3 data has been reproduced from prior work.[4] The inset indicates the incremental shifts in binding energies of the S 2p core-level features (for ZrS_3) with a decrease in temperature, at low temperatures.

gate voltage of 10 V is well away from the metal–nonmetal transition seen for TiS_3 at the higher applied gate voltages.[4] As seen in Figure 4, both temperature dependencies of the mobilities show clear maxima in the relative mobilities at ~180 K for TiS_3 and at ~218 K for ZrS_3. For each material, after the maximum, the mobility decreases with increasing temperature due to the increased phonon scattering.[4,9] The mobilities for semiconducting ZrS_3 are significantly lower than for semiconducting TiS_3, because ZrS_3 is more dielectric than TiS_3, and the contacts for the device here are not ohmic, unlike TiS_3.[11] So while the higher temperature for the onset of decreasing mobility and more gradual decline in mobility, seen for ZrS_3, could be a result of the very small mobilities being less sensitive to phonon scattering, key is that the measured ZrS_3 mobilities seem less sensitive to phonon scattering, even when one takes into account the higher temperature mobilities previously measured for ZrS_3.[9] This observation is fully consistent with the higher Debye temperatures obtained for ZrS_3 as compared to TiS_3. Furthermore, the decline in mobilities, seen here at higher temperatures for ZrS_3 and as reported elsewhere for ZrS_3,[9] follow a $T^{-3/2}$ law, which is characteristic of phonon scattering.

At lower temperatures, where the mobilities decrease with decreasing temperature, the situation is more complicated and electron–phonon scattering does not tell the entire story. The TiS_3 and ZrS_3 samples become increasingly dielectric[4,9] indicative of a loss of carriers while the mobility further decreases as the ionized-dopant scattering rate is found to increase with decreases in temperature, as is seen in the case of TiS_3.[4] This is evident from the increase in XPS binding energies at lower temperatures, as plotted for ZrS_3 in the inset to Figure 4. That said, electron–phonon scattering appears to outweigh other scattering processes at high enough temperatures (temperatures in the vicinity of room temperature).[4,9]

Several routes to the suppression of critical soft modes are indicated, including the overcoating of the transistor with a stiff dielectric. The possibility of such manipulation of the lattice rigidity is indicated by the increase in mobility measured in transistors overcoated with Al_2O_3.[12]

In conclusion, Debye–Waller plots for the temperature-dependent S 2p core-level photoemission intensities of TiS_3 and ZrS_3 indicate different effective Debye temperatures for the different sulfur species S^{2-} and S_2^{2-} present in these trichalcogenides. The differences in the effective Debye temperatures of different sulfur species within a system may be attributed to the difference in their coordination. Moreover, the difference between the metal–sulfur ionic bond strengths of TiS_3 and ZrS_3 can be seen on comparing the effective Debye temperature of the two sulfur species of TiS_3 with ZrS_3. Thus, comparatively higher effective sulfur Debye temperatures for ZrS_3 are consistent with the more-ionic Zr–S bonds. The comparison of temperature dependence of the measured carrier mobilities for TiS_3 and ZrS_3 is consistent with the measured Debye temperatures. These findings provide a better quantitative understanding of phonon scattering in these systems and suggest that there are only a limited number of soft phonon modes that otherwise seem to be represented by a stiff lattice.

■ ASSOCIATED CONTENT

Supporting Information

The Supporting Information is also presented. The Supporting Information is available free of charge at https://pubs.acs.org/doi/10.1021/acsmaterialslett.1c00094.

X-ray photoemission of the S 2p core level, with the S^{2-} and S_2^{2-} components indicated, as a function of temperature; atomic force microscopy (AFM) image and height profile of a working ZrS_3 device on SiO_2 (PDF)

■ AUTHOR INFORMATION

Corresponding Author

Peter A. Dowben – *Department of Physics and Astronomy, University of Nebraska–Lincoln, Lincoln, Nebraska 68588-0299, United States;* orcid.org/0000-0002-2198-4710; Email: pdowben1@unl.edu

Authors

Archit Dhingra – *Department of Physics and Astronomy, University of Nebraska–Lincoln, Lincoln, Nebraska 68588-0299, United States*

Alexey Lipatov – *Department of Chemistry, University of Nebraska, Lincoln, Nebraska 68588-0304, United States;* orcid.org/0000-0001-5043-1616

Michael J. Loes – *Department of Chemistry, University of Nebraska, Lincoln, Nebraska 68588-0304, United States*

Alexander Sinitskii – *Department of Chemistry, University of Nebraska, Lincoln, Nebraska 68588-0304, United States;* orcid.org/0000-0002-8688-3451

Complete contact information is available at: https://pubs.acs.org/10.1021/acsmaterialslett.1c00094

Author Contributions

The manuscript was written through contributions of all authors. All authors have given approval to the final version of the manuscript.

Funding

This research was supported by the National Science Foundation (NSF), through Grant No. NSF-ECCS 1740136,

and nCORE, a wholly owned subsidiary of the Semiconductor Research Corporation (SRC), task #2760.002.

Notes

The authors declare no competing financial interest.

■ ACKNOWLEDGMENTS

This research was supported by the National Science Foundation (NSF), through Grant No. NSF-ECCS 1740136, as well as by the nCORE, which is a wholly owned subsidiary of the Semiconductor Research Corporation (SRC), through the Center on Antiferromagnetic Magneto-electric Memory and Logic Task No. 2760.002.

■ ABBREVIATIONS

TMD, transition-metal dichalcogenide; TMT, transition-metal trichalcogenide; XPS, X-ray photoemission

■ REFERENCES

(1) Dai, J.; Zeng, X. C. Titanium Trisulfide Monolayer: Theoretical Prediction of a New Direct-Gap Semiconductor with High and Anisotropic Carrier Mobility. *Angew. Chem., Int. Ed.* **2015**, *54* (26), 7572−7576.

(2) Ahammed, R.; Rawat, A.; Jena, N.; Dimple; Mohanta, M. K.; De Sarkar, A. ZrS_3/MS_2 and ZrS_3/MXY (M = Mo, W; X, Y = S, Se, Te; X ≠ Y) Type-II van Der Waals Hetero-Bilayers: Prospective Candidates in 2D Excitonic Solar Cells. *Appl. Surf. Sci.* **2020**, *499*, 143894.

(3) Wang, C.; Zheng, C.; Gao, G. Bulk and Monolayer ZrS_3 as Promising Anisotropic Thermoelectric Materials: A Comparative Study. *J. Phys. Chem. C* **2020**, *124* (12), 6536−6543.

(4) Randle, M.; Lipatov, A.; Kumar, A.; Kwan, C.-P.; Nathawat, J.; Barut, B.; Yin, S.; He, K.; Arabchigavkani, N.; Dixit, R.; et al. Gate-Controlled Metal-Insulator Transition in TiS_3 Nanowire Field-Effect Transistors. *ACS Nano* **2019**, *13* (1), 803−811.

(5) Island, J. O.; Biele, R.; Barawi, M.; Clamagirand, J. M.; Ares, J. R.; Sánchez, C.; Van Der Zant, H. S. J.; Ferrer, I. J.; D'Agosta, R.; Castellanos-Gomez, A. Titanium Trisulfide (TiS_3): A 2D Semiconductor with Quasi-1D Optical and Electronic Properties. *Sci. Rep.* **2016**, *6*, 22214.

(6) Island, J. O.; Buscema, M.; Barawi, M.; Clamagirand, J. M.; Ares, J. R.; Sánchez, C.; Ferrer, I. J.; Steele, G. A.; van der Zant, H. S. J.; Castellanos-Gomez, A. Ultrahigh Photoresponse of Few-Layer TiS_3 Nanoribbon Transistors. *Adv. Opt. Mater.* **2014**, *2* (7), 641−645.

(7) Island, J. O.; Barawi, M.; Biele, R.; Almazán, A.; Clamagirand, J. M.; Ares, J. R.; Sánchez, C.; Van Der Zant, H. S. J.; Álvarez, J. V.; D'Agosta, R.; et al. TiS_3 Transistors with Tailored Morphology and Electrical Properties. *Adv. Mater.* **2015**, *27* (16), 2595−2601.

(8) Molina-Mendoza, A. J.; Barawi, M.; Biele, R.; Flores, E.; Ares, J. R.; Sánchez, C.; Rubio-Bollinger, G.; Agraït, N.; D'Agosta, R.; Ferrer, I. J.; et al. Electronic Bandgap and Exciton Binding Energy of Layered Semiconductor TiS_3. *Adv. Electron. Mater.* **2015**, *1* (9), 1500126.

(9) Perluzzo, G.; Lakhani, A. A.; Jandl, S. Electrical Transport Measurements in a Quasi-One Dimensional Semiconductor ZrS_3. *Solid State Commun.* **1980**, *35* (3), 301−304.

(10) Späh, R.; Lux-Steiner, M.; Bucher, E.; Wagner, S. n-ZrS_3/ p-WSe_2 heterojunctions. *Appl. Phys. Lett.* **1984**, *45* (7), 744−745.

(11) Gilbert, S. J.; Lipatov, A.; Yost, A. J.; Loes, M. J.; Sinitskii, A.; Dowben, P. A. The Electronic Properties of Au and Pt Metal Contacts on Quasi-One-Dimensional Layered TiS_3(001). *Appl. Phys. Lett.* **2019**, *114* (10), 101604.

(12) Lipatov, A.; Wilson, P. M.; Shekhirev, M.; Teeter, J. D.; Netusil, R.; Sinitskii, A. Few-Layered Titanium Trisulfide (TiS_3) Field-Effect Transistors. *Nanoscale* **2015**, *7* (29), 12291−12296.

(13) Wimmer, M.; Adagideli, Đ.; Berber, S.; Tománek, D.; Richter, K. Spin Currents in Rough Graphene Nanoribbons: Universal Fluctuations and Spin Injection. *Phys. Rev. Lett.* **2008**, *100* (17), 177207.

(14) Han, M. Y.; Brant, J. C.; Kim, P. Electron Transport in Disordered Graphene Nanoribbons. *Phys. Rev. Lett.* **2010**, *104* (5), 056801.

(15) Dubois, S. M. M.; Lopez-Bezanilla, A.; Cresti, A.; Triozon, F.; Biel, B.; Charlier, J. C.; Roche, S. Quantum Transport in Graphene Nanoribbons: Effects of Edge Reconstruction and Chemical Reactivity. *ACS Nano* **2010**, *4* (4), 1971−1976.

(16) Jensen, S. A.; Ulbricht, R.; Narita, A.; Feng, X.; Müllen, K.; Hertel, T.; Turchinovich, D.; Bonn, M. Ultrafast Photoconductivity of Graphene Nanoribbons and Carbon Nanotubes. *Nano Lett.* **2013**, *13* (12), 5925−5930.

(17) Patra, A.; Rout, C. S. Anisotropic Quasi-One-Dimensional Layered Transition-Metal Trichalcogenides: Synthesis, Properties and Applications. *RSC Adv.* **2020**, *10* (60), 36413−36438.

(18) Ferrer, I. J.; Ares, J. R.; Clamagirand, J. M.; Barawi, M.; Sánchez, C. Optical Properties of Titanium Trisulphide (TiS_3) Thin Films. *Thin Solid Films* **2013**, *535* (1), 398−401.

(19) Jin, Y.; Li, X.; Yang, J. Single Layer of MX_3 (M = Ti, Zr; X = S, Se, Te): A New Platform for Nano-Electronics and Optics. *Phys. Chem. Chem. Phys.* **2015**, *17* (28), 18665−18669.

(20) Yi, H.; Gilbert, S. J.; Lipatov, A.; Sinitskii, A.; Avila, J.; Abourahma, J.; Komesu, T.; Asensio, M. C.; Dowben, P. A. The Electronic Band Structure of Quasi-One-Dimensional van Der Waals Semiconductors: The Effective Hole Mass of ZrS_3 Compared to TiS_3. *J. Phys.: Condens. Matter* **2020**, *32* (29), 29LT01.

(21) Brattås, L.; Kjekshus, A.; Krogh-Moe, J.; Songstad, J.; Pilotti, Å. On the Properties of Compounds with the $ZrSe_3$ Type Structure. *Acta Chem. Scand.* **1972**, *26*, 3441−3449.

(22) Lipatov, A.; Loes, M. J.; Lu, H.; Dai, J.; Patoka, P.; Vorobeva, N. S.; Muratov, D. S.; Ulrich, G.; Kästner, B.; Hoehl, A.; et al. Quasi-1D TiS_3 Nanoribbons: Mechanical Exfoliation and Thickness-Dependent Raman Spectroscopy. *ACS Nano* **2018**, *12* (12), 12713−12720.

(23) Yi, H.; Komesu, T.; Gilbert, S.; Hao, G.; Yost, A. J.; Lipatov, A.; Sinitskii, A.; Avila, J.; Chen, C.; Asensio, M. C.; et al. The Band Structure of the Quasi-One-Dimensional Layered Semiconductor TiS_3(001). *Appl. Phys. Lett.* **2018**, *112* (5), 052102.

(24) Cui, Q.; Lipatov, A.; Wilt, J. S.; Bellus, M. Z.; Zeng, X. C.; Wu, J.; Sinitskii, A.; Zhao, H. Time-Resolved Measurements of Photocarrier Dynamics in TiS_3 Nanoribbons. *ACS Appl. Mater. Interfaces* **2016**, *8* (28), 18334−18338.

(25) Muratov, D. S.; Vanyushin, V. O.; Vorobeva, N. S.; Jukova, P.; Lipatov, A.; Kolesnikov, E. A.; Karpenkov, D.; Kuznetsov, D. V.; Sinitskii, A. Synthesis and Exfoliation of Quasi-1D $(Zr,Ti)S_3$ Solid Solutions for Device Measurements. *J. Alloys Compd.* **2020**, *815*, 152316.

(26) Muratov, D. S.; Ishteev, A. R.; Lypenko, D. A.; Vanyushin, V. O.; Gostishev, P.; Perova, S.; Saranin, D. S.; Rossi, D.; Auf Der Maur, M.; Volonakis, G.; et al. Slot-Die-Printed Two-Dimensional ZrS_3 Charge Transport Layer for Perovskite Light-Emitting Diodes. *ACS Appl. Mater. Interfaces* **2019**, *11* (51), 48021−48028.

(27) Dhingra, A.; Marzouk, Z. G.; Mishra, E.; Galiy, P. V.; Nenchuk, T. M.; Dowben, P. A. Indium Segregation to the Selvedge of In_3Se_3 (001). *Phys. B* **2020**, *593*, 412280.

(28) Wu, K.; Torun, E.; Sahin, H.; Chen, B.; Fan, X.; Pant, A.; Parsons Wright, D.; Aoki, T.; Peeters, F. M.; Soignard, E.; et al. Unusual Lattice Vibration Characteristics in Whiskers of the Pseudo-One-Dimensional Titanium Trisulfide TiS_3. *Nat. Commun.* **2016**, *7* (1), 12952.

(29) Osada, K.; Bae, S.; Tanaka, M.; Raebiger, H.; Shudo, K.; Suzuki, T. Phonon Properties of Few-Layer Crystals of Quasi-One-Dimensional ZrS_3 and $ZrSe_3$. *J. Phys. Chem. C* **2016**, *120* (8), 4653−4659.

(30) Ghasemi, F.; Frisenda, R.; Flores, E.; Papadopoulos, N.; Biele, R.; Perez de Lara, D.; van der Zant, H. S. J.; Watanabe, K.; Taniguchi, T.; D'Agosta, R.; et al. Tunable Photodetectors via In Situ Thermal Conversion of TiS_3 to TiO_2. *Nanomaterials* **2020**, *10* (4), 711.

(31) Waldfried, C.; McIlroy, D. N.; Zhang, J.; Dowben, P. A.; Katrich, G. A.; Plummer, E. W. Determination of the Surface Debye

https://doi.org/10.1021/acsmaterialslett.1c00094
ACS Materials Lett. 2021, 3, 414−419

Temperature of Mo(112) Using Valence Band Photoemission. *Surf. Sci.* **1996**, *363* (1−3), 296−302.
(32) Shevchik, N. J. Disorder Effects in Angle-Resolved Photoelectron Spectroscopy. *Phys. Rev. B* **1977**, *16* (8), 3428−3442.
(33) Clarke, L. J. *Surface Crystallography: An Introduction to Low Energy Electron Diffraction*; John Wiley & Sons, Inc., 1985.
(34) Van Hove, M. A.; Weinberg, W. H.; Chan, C. M. *Low-Energy Electron Diffraction*; Springer Series in Surface Science, 1986.
(35) Jeong, H.; Komesu, T.; Dowben, P.; Schultz, B.; Palmstrøm, C. The Anomalous Effective Surface Debye Temperature of ErAs (100). *Phys. Lett. A* **2002**, *302* (4), 217−223.
(36) Fukutani, K.; Sato, T.; Galiy, P. V.; Sugawara, K.; Takahashi, T. Tunable two-dimensional electron gas at the surface of thermoelectric material In_4Se_3. *Phys. Rev. B* **2016**, *93*, 205156.

https://doi.org/10.1021/acsmaterialslett.1c00094
ACS Materials Lett. 2021, 3, 414−419